

# Constraining Hot Plasma in a Non-flaring Solar Active Region with FOXSI Hard X-ray Observations

Shin-nosuke ISHIKAWA

National Astronomical Observatory of Japan, 2-21-1 Mitaka, Tokyo 181-8588, Japan  
s.ishikawa@nao.ac.jp

Lindsay GLESENER

Space Science Laboratory, University of California, Berkeley, CA 94720, USA  
glesener@ssl.berkeley.edu

Steven CHRISTE

NASA Goddard Space Flight Center, Greenbelt, MD 20771-0001, USA  
steven.d.christe@nasa.gov

Kazunori ISHIBASHI

Nagoya University, Furo-cho, Chikusa-ku, Nagoya, Aichi 464-8602, Japan  
bish@u.phys.nagoya-u.ac.jp

David H. BROOKS

College of Science, George Mason University, 4400 University Drive, Fairfax, VA 22030, USA  
dhbrooks@ssd5.nrl.navy.mil

David R. WILLIAMS

Mullard Space Science Laboratory, University College London, Holmbury St Mary, Surrey, RH5 6NT, UK  
d.r.williams@ucl.ac.uk

Masumi SHIMOJO

National Astronomical Observatory of Japan, 2-21-1 Mitaka, Tokyo 181-8588, Japan  
masumi.shimojo@nao.ac.jp

Nobuharu SAKO

National Astronomical Observatory of Japan, 2-21-1 Mitaka, Tokyo 181-8588, Japan  
sako@solar.mtk.nao.ac.jp

and

Säm KRUCKER

Space Science Laboratory, University of California, Berkeley, CA 94720, USA,  
and Institute of 4D Technologies, School of Engineering, University of Applied Sciences and Arts Northwestern Switzerland,  
5210 Windisch, Switzerland  
krucker@ssl.berkeley.edu

(Received ; accepted )

## Abstract

We present new constraints on the high-temperature emission measure of a non-flaring solar active region using observations from the recently flown *Focusing Optics X-ray Solar Imager* sounding rocket payload. *FOXSI* has performed the first focused hard X-ray (HXR) observation of the Sun in its first successful flight on 2012 November 2. Focusing optics, combined with small strip detectors, enable high-sensitivity observations with respect to previous indirect imagers. This capability, along with the sensitivity of the HXR regime to high-temperature emission, offers the potential to better characterize high-temperature plasma in the corona as predicted by nanoflare heating models. We present a joint analysis of the differential emission measure (DEM) of active region 11602 using coordinated observations by *FOXSI*, *Hinode*/XRT and *Hinode*/EIS. The *Hinode*-derived DEM predicts significant emission measure between 1 MK and 3 MK, with a peak in the DEM predicted at 2.0–2.5 MK. The combined XRT and EIS DEM also shows emission from a smaller population of plasma above 8 MK. This is contradicted by *FOXSI* observations that significantly constrain emission above 8 MK. This suggests that the *Hinode* DEM analysis has larger uncertainties at higher temperatures and that  $>8$  MK plasma above an emission measure of  $3 \times 10^{44} \text{ cm}^{-3}$  is excluded in this active region.

**Key words:** Sun: active region - Sun: particle emission - Sun: X-rays

## 1. Introduction

The energy source of the high-temperature corona is one of the main open questions in heliophysics. The two lead-

ing theoretical solutions are (1) heating by a large number of small-scale magnetic energy releases in the chromosphere and corona (so-called ‘nanoflare heating’) or (2) heating by waves that are excited below the photosphere and released in the chromosphere and corona (‘wave heating’). One of the main differences between these two models is the prediction of the time evolution of the plasma temperature as the heat input and output (e.g. radiative and conductive transfers) interact (e.g. Cargill & Klimchuk 2004; van Ballegoijen et al. 2011). This difference is most easily discerned by measuring the amount of plasma at each temperature through the differential emission measure (DEM) distribution from below one million up to  $\sim 20$  million Kelvin.

The most accurate DEM measurements are from non-flaring active regions (e.g. Reale et al. 2009; Patsourakos & Klimchuk 2009; O’Dwyer et al. 2011; Testa et al. 2011; Warren et al. 2011; Warren et al. 2012; Warren et al. 2013; Hannah & Kontar 2012) where non-equilibrium effects are potentially less important than during flares (e.g. Reale & Orlando 2008). Observations in the extreme ultra-violet (EUV), soft X-rays (SXR), and hard X-rays (HXR) provide constraints of the DEM in different temperature ranges. To get information over a wide temperature range, it is essential to combine multiwavelength observations.

Currently-available observations in the EUV by *Hinode* and the *Solar Dynamics Observatory (SDO)* provide accurate information about the low temperature plasma ( $< 8$  MK) but emission at the high-temperatures ( $> 8$  MK) is generally too weak to be detected by currently available EUV line observations. Past observations from *Hinode*’s EUV Imaging Spectrometer (EIS) have characterized the DEM in the few million Kelvin range (e.g. Warren et al. 2012) and have found a DEM for non-flaring active regions with a peak around  $\sim 4$  MK. The observed slope of the DEM is rather steep, favoring wave heating models. EUV and SXR broadband filter observations cover a wider range in temperature, but observations are not without intrinsic biases (e.g. Schmelz et al. 2009b; Winebarger et al. 2012; Guennou et al. 2013). Besides the few-MK component in non-flaring active regions, EUV and SXR filter observations suggest the existence of an additional, hotter component that is speculated to be a direct signature of nanoflare heating (e.g. Reale et al. 2009; Schmelz et al. 2009a; Testa & Reale 2012), although not without controversy (e.g. Schmelz et al. 2009b; Winebarger et al. 2012). Others report no significant component above the sensitivity limit of these instruments (e.g. Testa et al. 2011). In any case, current observations show that an additional hot component, if present, is much weaker than the main emission around a few MK, making an unambiguous detection difficult. Observations of a high temperature component is limited as currently-available EUV and SXR instrumentation have ‘blind spots’ at higher temperatures (Winebarger et al. 2012), particularly for non-flaring observations that have an intrinsically low high-temperature emission measure. Future observations of high-temperature SXR lines have the potential to signif-

icantly improve high-temperature diagnostics, and appropriate instrumentation is under development (Kobayashi et al. 2011).

To restrict high-temperature ( $> 8$  MK) plasma, X-ray observations of the thermal bremsstrahlung emission of hot electrons provide excellent sensitivity (e.g. McTiernan 2009; Reale et al. 2009; Miceli et al. 2012). By combining EUV and SXR diagnostics with observations in HXR from the *Reuven Ramaty High Energy Spectroscopic Imager (RHESSI)* (Lin et al. 2002), the high-temperature component in an active region DEM is sometimes significantly restricted, indicating that EUV and SXR alone can overestimate hot emissions (Schmelz et al. 2009b), in particular in the presence of strong emissions at lower temperatures. Using X-ray observations only, McTiernan (2009) showed that there are indeed non-flaring times (defined as times without a *GOES* flare) with a significant 5-10 MK component in the DEM. Since the appearance of this component scales with the solar cycle, it is, however, unclear whether the observed component is due to unresolved microflares not excluded in the selection of non-flaring times or due to continuous heating relevant to overall coronal heating. Unfortunately, *RHESSI* observations provide only limited sensitivity due to the high nonsolar background of its bulk germanium detectors.

In this paper, we present an active region measured in HXR with greatly enhanced sensitivity using focusing optics on the recently flown *Focusing Optics X-ray Solar Imager (FOXSI)* sounding rocket payload. *FOXSI* is funded under NASA’s Low Cost Access to Space (LCAS) program and is the first example of HXR focusing optics applied to solar observation. *FOXSI* is a HXR imaging spectrometer operating in the energy range of 4–15 keV, with an angular resolution of  $\sim 9$  arcseconds (on-axis) and an energy resolution of  $\sim 0.5$  keV (Krucker et al. 2013).

*FOXSI* flew for the first time, successfully, on 2012 November 2 from the White Sands Missile Range in New Mexico, USA (Krucker et al. 2014). Targets included active regions on the disk and quiet portions of the Sun. A microflare (*GOES* class B2.7) was observed by *FOXSI* on the western limb (Krucker et al. 2013), serving as useful in-flight calibration of the instrument, since it was also observed by *RHESSI*. In this paper we report on the *FOXSI* observation of active region 11602 in the  $> 4$  keV range and compare to EUV and SXR observations from the *Hinode* (Kosugi et al. 2007) EUV Imaging Spectrometer (EIS, Culhane et al. 2007) and X-ray Telescope (XRT, Golub et al. 2007) to constrain a potential hot component.

## 2. Observations

*FOXSI* observed the Sun beginning at 2012 November 2 17:56:48 UT for a total of 6.5 minutes, with 44 seconds of observation time on active region (AR) 11602 (its first target). Observations were coordinated with the *Hinode* spacecraft (*Hinode* Operation Plan #221). *Hinode* observed AR 11602 before and after the *FOXSI* launch, from 16:44 to 17:50 UT and from 19:00 to 20:15 UT. The XRT and EIS instruments ran programs appropri-

ate for the measurement of active region DEMs with multiple XRT filter pairs and multiple EIS wavelength bands to cover the temperature range of  $\log T \sim 5.5 - 7.2$ . The EIS line set covered the temperature range up to  $\log T \sim 7.2$  (Fe XXIV). Emissions from the high-temperature lines ( $\log T \geq 7.0$ ) are generally weak and blended with stronger, low temperature lines. Usually, these lines are only detected in flaring regions, and lines with temperatures above  $\log T \sim 6.8$  are not customarily detected, as described in Section 2.2. From 17:50 to 19:00 (including the *FOXSI* observation period), *Hinode* pointed to a quiescent region in the northwest of the solar disk in order to support *FOXSI*'s quiet-Sun investigation.

### 2.1. *Hinode* XRT

XRT observed AR 11602 with multiple filters. A set of images composed of 11 filter pairs were taken every 20 minutes with a field of view (FOV) of  $2048'' \times 2048''$  and  $4'' \times 4''$  resolution ( $4 \times 4$  CCD pixel binning). XRT images combining short and long exposures with the thin and thick filters (Al mesh and Al thick) are shown in the upper panels of Figure 1. Significant emission is clearly detected with the Al thick filter. For the purposes of this paper the core of the active region is defined as the rectangular area shown in cyan in Figure 1 (with corners  $[-365, -500]$  arcseconds and  $[-245, -380]$  arcseconds in helioprojective coordinates). This region is used for the analysis and discussion below. Using the standard SolarSoft procedure `xrt_prep.pro`, we removed cosmic ray spikes and CCD biases, but we did not apply the Fourier clean and vignetting removal because they introduce uncertainties and the region of interest is almost at the center of the FOV. After applying the dark current model using `xrt_prep.pro`, we applied a further correction to set the zero-point at the median value of the lowest 5 CCD rows since these pixels are below the shielding material and not affected by the sky events. The averaged count rate for each filter pair in the region is shown in Table 1.

### 2.2. *Hinode* EIS

EIS observed the active region using the 1-arcsecond-wide slit scanning over the region, for an FOV of  $120 \times 512$  arcsecond<sup>2</sup> for the complete raster. EIS took spectra in 25 wavelength windows with spatial sampling every 1 arcsec in the solar-Y direction (along the slit) and scanned every 2 arcsec in the solar-X direction. The slit scan was performed twice: once from 16:44 to 17:44 UT and again from 19:14 to 20:14 UT. The observed intensity map of the Fe XII line ( $\log T \sim 6.1$ ) for the first observation is shown in the lower left panel of Figure 1.

Values for all observed EIS lines are listed in Table 2. The EIS data were calibrated using the pre-launch calibration (Lang et al. 2006), and then the Warren et al. (2013b) time-dependent correction was applied. The values were obtained via Gaussian fits to the line profiles using spatially averaged spectra. Lines that are not clearly detected or are possibly blended are excluded from this table and from our analysis, except the Ca XVII line. The Ca XVII line was kept because it is expected to be sensitive to the

highest temperatures of any line in this EIS set; its intensity is derived using the method of Ko et al. (2009). In total, lines sensitive to temperatures from  $\log T \sim 5.6$  to 6.8 were detected. The plasma density can be estimated from the ratio of a pair of lines with an identical ion, such as the Fe XII 186.88 / 195.12 Å ratio (Young et al. 2007). From this ratio, the coronal plasma density in the active region is estimated to be  $1.6 \times 10^9 \text{ cm}^{-3}$ .

### 2.3. *FOXSI*

*FOXSI* pairs seven direct-focusing optics modules with a dedicated silicon strip detector for each. Each optics module is composed of seven Wolter-I mirrors produced using an electroformed nickel replication process at MSFC (Ramsey et al. 2002; Ramsey 2006). The detectors are double-sided silicon detectors designed at ISAS (Ishikawa et al. 2011) and are based on the detector development for the Hard X-ray Telescope aboard the *Astro-H* spacecraft (Kokubun et al. 2012). More detail on the *FOXSI* instrument and its first flight can be found in Krucker et al. (2013) and Krucker et al. (2014). Data are collected independently from the seven detectors, so each optic/detector pair provides an independent measurement.

During *FOXSI*'s first flight, AR 11602 was observed during the first target pointing for 44 seconds. The FOV is limited both by the off-axis response of the optics and the physical size of the detector. The detector active area is  $9.6 \times 9.6 \text{ mm}^2$ , allowing a FOV of 16.5 arcminutes. Because of imperfect alignment between the instrument and the rocket's pointing system, the on-axis position of the optics modules was located approximately 2 arcminutes from the pointing center of the rocket. This offset was determined in-flight by comparing the microflare position as observed by *FOXSI* and by *RHESSI*. The active region center was located  $\sim 3$  arcminutes from the rocket pointing center, or  $\sim 5$  arcminutes from the optics axis. At 5 arcminutes off-axis, the optics efficiency is  $\sim 85\%$  of the nominal on-axis value; this factor has been included in the instrument response.

The optics modules were covered on both ends by thermal blankets composed of kapton and aluminized mylar to avoid thermal distortions of the mirror modules. In addition to those nominal blankets, additional thermal blanketing material (located on the inner surface of the telescope metering structure) moved into and blocked the optical path sometime during the flight, reducing the effective area from its nominal value, mostly at low energies. The effect of this additional blanketing is estimated by comparing observed *FOXSI* and *RHESSI* thermal spectra from the microflare (which was observed by *FOXSI* during the second half of its observing time). *RHESSI* measures a total emission measure of  $4.8 \pm 1.0 \times 10^{46} \text{ cm}^{-3}$  and an electron temperature of  $9.4 \pm 0.4 \text{ MK}$  for this microflare. Based on the *RHESSI* observed parameters, expected *FOXSI* count spectra were computed and compared with the measured values, yielding the actual spectral response of the instrument in-flight. From this analysis, we estimate that *FOXSI* counts were reduced to 11% and 24% of their nominal values for the 6-7 and 7-8 keV

**Table 1.** Observed active region XRT counts used for the DEM analysis.

Filter pair	Count rate [DN s <sup>-1</sup> pixel <sup>-1</sup> ]*	Predicted count rate <sup>+</sup> [DN s <sup>-1</sup> pixel <sup>-1</sup> ]*
Open / Be thick	0.00663	0.00728
Open / Al thick	0.173	0.368
Open / Ti poly	207	142
Open / Al mesh	498	347
Al poly / Ti poly	114	83.1
C poly / Ti poly	87.1	68.2
C poly / Open	279	219
Be thin / Open	11.5	51.0
Be med / Open	6.99	8.93
Al med / Open	3.80	4.10
Al poly / Open	389	297

(\*) Per single pixel of the XRT CCD ( $\sim 1'' \times 1''$ ), not an area element of the  $4 \times 4$  binning. (+) Predicted XRT count rates derived from the DEM solution.

**Table 2.** Observed EIS line intensities at the active region used for the DEM analysis. Shown line wavelengths and temperatures are from Culhane et al. 2007, Young et al. 2007 and Young 2009.

Ion	Wavelength [Å]	Temperature log $T$ [K]	Intensity [erg cm <sup>-2</sup> s <sup>-1</sup> str <sup>-1</sup> ]	Predicted intensity <sup>+</sup> [erg cm <sup>-2</sup> s <sup>-1</sup> str <sup>-1</sup> ]
Fe VIII	185.21	5.6	217	211
Fe VIII	186.60	5.6	118	111
Fe IX	197.86	5.9	47.7	62.5
Fe X	184.54	6.0	374	292
Fe XI	180.40	6.1	1474	1445
Fe XI	182.16	6.1	303	281
Fe XII	186.88	6.1	534	439
Fe XII	195.12	6.1	1221	1339
Si X	258.37	6.1	288	364
Fe XIII	201.13	6.2	485	362
Fe XIII	202.04	6.2	1072	700
S X	264.23	6.2	80.6	110
Fe XIV	264.79	6.3	540	708
Fe XIV	270.52	6.3	336	363
Fe XV	284.16	6.3	4760	4726
S XIII	256.68	6.4	293	389
Fe XVI	262.98	6.4	232	182
Ca XIV	193.87	6.5	24.3	17.2
Ca XVII	192.86	6.8	18.6	3.31

(+) Predicted EIS intensities derived from the DEM solution.

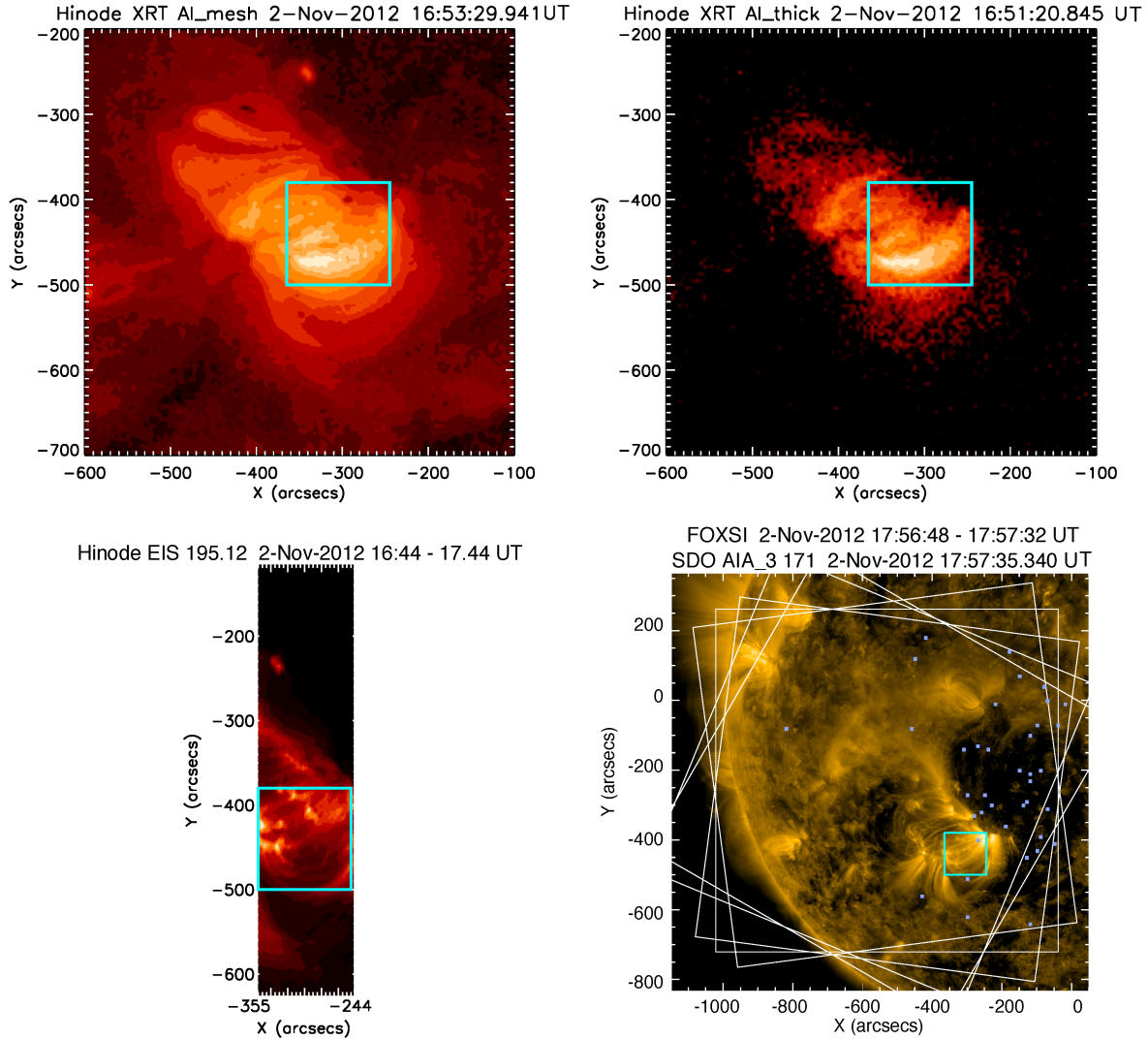


**Fig. 1.** Images of the active region from *Hinode*/XRT, *Hinode*/EIS, *SDO*/Atmospheric Imaging Assembly (AIA) and *FOXSI*. Top row: XRT images on log scales with the (left) Al mesh filter and (right) Al thick filter. Lower left: EIS intensity map of the Fe XII 195.12 Å line ( $\log T \sim 6.1$ ). Lower right: *SDO*/AIA 171 Å image overlaid with the *FOXSI* observed counts from five detectors, collected over 44 seconds. The field of view of each detector is shown by a white box.

bands by the excess blanketing. These factors have been included in the instrument response for the results presented here.

It is also possible to perform a rough self-calibration of the additional blanketing absorption by deriving temperatures from ratios of *FOXSI* fluxes at different energies. By requiring that the derived temperatures are constant across the observed energy range, we can fit the additional absorption for each detector. Temperatures derived in this way agree with those derived from *RHESSI* data, confirming those results. Details of this calibration will be shown in a following paper.

All seven detectors measured low count rates during the observation of AR 11602. The lower right panel of Figure 1 shows the positions of all 4-15 keV photons measured by detectors 0, 2, 4, 5 and 6, a total of 38 counts.

Two of the seven detectors were excluded from this analysis. Detector 1 showed excess noise on one half of the FOV due to a noisy readout ASIC; since this noise would interfere with the measurement of faint signals this detector was excluded. Detector 3 was excluded because the corresponding optic shifted during launch; this was noted by visual inspection post-flight and is responsible for a blurring of the flare image. For this portion of the flight, one detector (#4) measured a significantly higher count rate than the other detectors, leading us to believe that this detector was blocked by the least amount of additional blanketing.



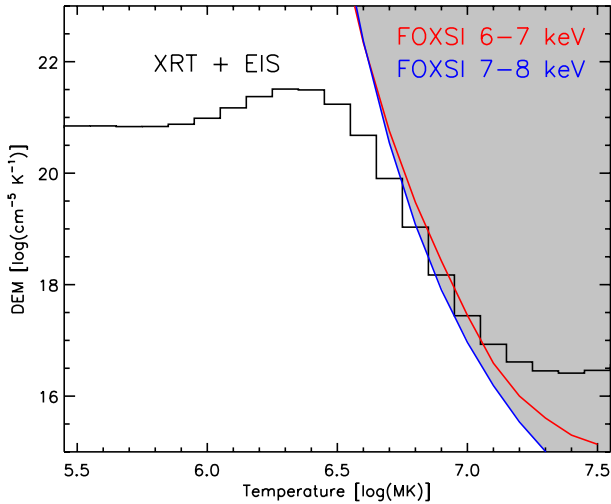


**Fig. 2.** *FOXSI* loci curve in two energy bands (red and blue) overlaid on a differential emission measure of the active region estimated by *Hinode*/XRT and EIS (black). The shaded region shows the parameter space that is excluded by the *FOXSI* observation.

### 3. Analysis and Discussion

Figure 2 shows the DEM as estimated from combined *Hinode* EIS and XRT observations of the active region, with *FOXSI* loci curves overlaid.

The combined *Hinode* DEM was calculated using the CHIANTI database and inversion technique (Monsignori Fossi & Landini 1991, the SSWIDL procedure `chianti_dem.pro`). This code is basically designed for line spectroscopy, and we modified the code to input the XRT count rates and temperature response functions. We assumed the measurement reliabilities of the EIS line intensities and XRT count rates are similar, and all the XRT and EIS measurements are equally weighted in the inversion. We applied the latest XRT calibration by Narukage et al. (2014), which provides a significantly upgraded XRT response function, especially for the thicker filters. The peak in the *Hinode* DEM is located at  $\log T \sim 6.3$ - $6.4$ , suggesting the main coronal component of this active region is  $\sim 2$ - $2.5$  MK plasma. The combined XRT and EIS DEM also shows the presence of an extremely hot component with a temperature  $> 10$  MK.

The counts measured by *FOXSI* (shown spatially in Figure 1) do not come from the active region; rather, they are spread across the field of view. These counts could be quiet-Sun flux or instrument artifacts (for example, single-bounce photons (‘ghost rays’) from the microflare on the west limb, which had already begun at the time of this pointing but which was well outside *FOXSI*’s FOV at the time); this determination will be the focus of a separate paper. In either case these counts constitute a background for the measurement of HXRs from the AR. The number of counts in any given energy band are so small that precise background statistics cannot be determined. We therefore assume that an AR HXR source would be detected if it produced a number of counts equal to the total

number of counts in the image; this is a conservative estimate. Dividing the counts into 1 keV bins, we calculate the emission measure required for a variety of temperatures to produce the measured counts in each bin. This produces a loci curve for the DEM for each 1 keV bin. Curves in Figure 2 show these loci for the 6-7 and 7-8 keV bands.

We find that the *Hinode*-derived hot ( $> 8$  MK) component in the DEM is inconsistent with the *FOXSI* observations in the gray area in Figure 2. If there is plasma with a DEM distribution extended into this region, *FOXSI* should have detected far more flux from the AR. The hot component as derived mainly by XRT would have produced  $> 1300$  counts in the *FOXSI* spectrum above 6 keV, but none were detected. A similar result was found by Schmelz et al. (2009b). After including *RHESSI* HXR upper limits in a DEM analysis, they found that their originally reported high temperature component was greatly suppressed. Winebarger et al. (2012) reports that the currently available EUV and SXR observatories have blind spots to high temperature plasma, at least in the presence of an intense component around a few MK as seen in non-flaring active regions. In addition, Testa et al. (2012) pointed out possible discrepancies between estimated DEMs from the EUV observations by comparing models and DEMs calculated by simulated *Hinode*/EIS and *SDO*/AIA data. The *FOXSI* observations highlight this issue and demonstrate the necessity of HXR observations to constrain the high-temperature end of the DEM.

The additional blanketing in the *FOXSI* instrument (see Section 2.3) is impossible to perfectly calibrate because the degree of absorption could have changed in time due to further physical motions of the blankets. Nevertheless, at high photon energies ( $> 10$  keV) where the blanket material contributes little absorption, the hot component derived mainly from XRT still predicts measured counts above 10 keV of a total of  $> 200$  counts, far more than were actually recorded. Hence, the blanketing issue alone cannot account for the discrepancies between *FOXSI* and *Hinode*, and these discrepancies are not influenced by the cross-calibration with *RHESSI*.

### 4. Summary and Future Work

We performed an active region DEM analysis using *Hinode*/XRT and EIS, and compared it to *FOXSI* detection limits as indicated by the *FOXSI* loci curves. We find an inconsistency between the *Hinode* DEM and the *FOXSI* limits for the hot, faint portion of the DEM with  $T > 8$  MK. We conclude that the  $> 8$  MK component above  $3 \times 10^{44} \text{ cm}^{-3}$  is excluded from the DEM since the *FOXSI* detector performance is validated via the co-observation of a microflare with *RHESSI*.

A second flight of *FOXSI* (*FOXSI*-2) is scheduled for December 2014 and will include some upgrades. *FOXSI*-2 will provide an improvement to optics by including additional small-diameter shells. In addition, we might update the detector by replacing some of the detectors with cadmium telluride double-sided strip detectors (Watanabe et

al. 2009; Ishikawa et al. 2010). To avoid the issue of excess material in the optical path, inner thermal blankets will be removed, and so we therefore expect a combined increase in sensitivity relative *FOXSI-1* by about an order of magnitude. A future spacecraft based on the *FOXSI* technology would have the necessary sensitivity to systematically image hot components in non-flaring active regions, or set stringent upper limits to be used to distinguish different coronal heating models.

### Acknowledgment

*FOXSI* was funded by NASA's LCAS program, grant NNX11AB75G. We would like to thank Dr. Kyoung-Sun Lee for her help with the EIS DEM analysis. The work was supported through a Grant-in-Aid for JSPS Fellows from Japan Society for the Promotion of Science. Work at UC Berkeley received support from NASA GSRP fellowship NNX09AM40H. *Hinode* is a Japanese mission developed and launched by ISAS/JAXA, collaborating with NAOJ as a domestic partner, NASA and STFC (UK) as international partners. Scientific operation of the *Hinode* mission is conducted by the *Hinode* science team organized at ISAS/JAXA. This team mainly consists of scientists from institutes in the partner countries. Support for the post-launch operation is provided by JAXA and NAOJ (Japan), STFC (U.K.), NASA, ESA, and NSC (Norway).

### References

- Bryans, P., Landi, E., & Savin, D. W. 2009, *ApJ*, 691, 1540  
 Cargill, P. J., & Klimchuk, J. A. 2004, *ApJ*, 605, 911  
 Culhane, J. L., Harra, L. K., James, A. M., et al. 2007, *Sol. Phys.*, 243, 19  
 Guennou, C., Auchère, F., Klimchuk, J. A., Bocchialini, K., & Parenti, S. 2013, *ApJ*, 774, 31  
 Golub, L., Deluca, E. E., Sette, A., & Weber, M. 2004, *The Solar-B Mission and the Forefront of Solar Physics*, 325, 217  
 Golub, L., Deluca, E., Austin, G., et al. 2007, *Sol. Phys.*, 243, 63  
 Hannah, I. G., & Kontar, E. P. 2012, *A&A*, 539, A146  
 Ishikawa, S., Watanabe, S., Fukuyama, T., et al. 2010, *Japanese Journal of Applied Physics*, 49, 116702  
 Ishikawa, S., Saito, S., Tajima, H., et al. 2011, *IEEE Transactions on Nuclear Science*, 58, 2039  
 Ko, Y.-K., Doschek, G. A., Warren, H. P., & Young, P. R. 2009, *ApJ*, 697, 1956  
 Kobayashi, K., Cirtain, J., Golub, L., et al. 2011, *Proc. SPIE*, 8147  
 Kokubun, M., Nakazawa, K., Enoto, T., et al. 2012, *Proc. SPIE*, 8443  
 Kosugi, T., Matsuzaki, K., Sakao, T., et al. 2007, *Sol. Phys.*, 243, 3  
 Krucker, S., Benz, A. O., Bastian, T. S., & Acton, L. W. 1997, *ApJ*, 488, 499  
 Krucker, S., Christe, S., Glesener, L., et al. 2013, *Proc. SPIE*, 8862  
 Krucker, S., Christe, S., Glesener, L., et al. 2014, *ApJL*, *submitted*  
 Landi, E., Del Zanna, G., Young, P. R., Dere, K. P., & Mason, H. E. 2012, *ApJ*, 744, 99  
 Lang, J., Kent, B. J., Paustian, W., et al. 2006, *Appl. Opt.*, 45, 8689  
 Lin, R. P., Dennis, B. R., Hurford, G. J., et al. 2002, *Sol. Phys.*, 210, 3  
 Masuda, S., Kosugi, T., Hara, H., Tsuneta, S., & Ogawara, Y. 1994, *Nature*, 371, 495  
 McTiernan, J. M. 2009, *ApJ*, 697, 94  
 Miceli, M., Reale, F., Gburek, S., et al. 2012, *A&A*, 544, A139  
 Monsignori Fossi, B. C., & Landini, M. 1991, *Advances in Space Research*, 11, 281  
 Narukage, N., Sakao, T., Kano, R., et al. 2014, *Sol. Phys.*, 289, 1029  
 O'Dwyer, B., Del Zanna, G., Mason, H. E., et al. 2011, *A&A*, 525, A137  
 Patsourakos, S., & Klimchuk, J. A. 2009, *ApJ*, 696, 760  
 Ramsey, B. D., Alexander, C. D., Apple, J. A., et al. 2002, *ApJ*, 568, 432  
 Ramsey, B. D. 2006, *Advances in Space Research*, 38, 2985  
 Reale, F., & Orlando, S. 2008, *ApJ*, 684, 715  
 Reale, F., Testa, P., Klimchuk, J. A., & Parenti, S. 2009, *ApJ*, 698, 756  
 Reale, F., McTiernan, J. M., & Testa, P. 2009, *ApJL*, 704, L58  
 Schmelz, J. T., Saar, S. H., DeLuca, E. E., et al. 2009, *ApJL*, 693, L131  
 Schmelz, J. T., Kashyap, V. L., Saar, S. H., et al. 2009, *ApJ*, 704, 863  
 Schmelz, J. T., Kimble, J. A., & Saba, J. L. R. 2012, *ApJ*, 757, 17  
 Testa, P., Reale, F., Landi, E., DeLuca, E. E., & Kashyap, V. 2011, *ApJ*, 728, 30  
 Testa, P., & Reale, F. 2012, *ApJL*, 750, L10  
 Testa, P., De Pontieu, B., Martínez-Sykora, J., Hansteen, V., & Carlsson, M. 2012, *ApJ*, 758, 54  
 van Ballegooijen, A. A., Asgari-Targhi, M., Cranmer, S. R., & DeLuca, E. E. 2011, *ApJ*, 736, 3  
 Warren, H. P., Brooks, D. H., & Winebarger, A. R. 2011, *ApJ*, 734, 90  
 Warren, H. P., Winebarger, A. R., & Brooks, D. H. 2012, *ApJ*, 759, 141  
 Warren, H. P., Mariska, J. T., & Doschek, G. A. 2013, *ApJ*, 770, 116  
 Warren, H. P., Ugarte-Urra, I., & Landi, E. 2013b, *arXiv:1310.5324*  
 Watanabe, S., Ishikawa, S.-N., Aono, H., et al. 2009, *IEEE Transactions on Nuclear Science*, 56, 777  
 Winebarger, A. R., Warren, H. P., Schmelz, J. T., et al. 2012, *ApJL*, 746, L17  
 Weber, M. A., Deluca, E. E., Golub, L., & Sette, A. L. 2004, *Multi-Wavelength Investigations of Solar Activity*, 223, 321  
 Young, P. R., Del Zanna, G., Mason, H. E., et al. 2007, *PASJ*, 59, 857  
 Young, P. R. 2009, *ApJL*, 691, L77